

Contents lists available at [SciVerse ScienceDirect](http://www.sciencedirect.com)

Energy

journal homepage: www.elsevier.com/locate/energy

Cloud detection, classification and motion estimation using geostationary satellite imagery for cloud cover forecast

H. Escrig^b, F.J. Batlles^{a,b,*}, J. Alonso^b, F.M. Baena^b, J.L. Bosch^b, I.B. Salbidegoitia^c, J.I. Burgaleta^c

^a Department of Applied Physics, University of Almería, 04120 Almería, Spain

^b CIESOL, Joint Centre University of Almería-CIEMAT, 04120 Almería, Spain

^c Torresol Energy Investments S.A. Avda. Zugazarte 61, 48930 Getxo (Vizcaya), Spain

ARTICLE INFO

Article history:

Received 28 November 2012

Received in revised form

25 January 2013

Accepted 28 January 2013

Available online xxx

Keywords:

Solar radiation forecasting

Meteosat Second Generation

Cloud motion detection

ABSTRACT

Considering that clouds are the greatest causes to solar radiation blocking, short term cloud forecasting can help power plant operation and therefore improve benefits. Cloud detection, classification and motion vector determination are key to forecasting sun obstruction by clouds. Geostationary satellites provide cloud information covering wide areas, allowing cloud forecast to be performed for several hours in advance. Herein, the methodology developed and tested in this study is based on multispectral tests and binary cross correlations followed by coherence and quality control tests over resulting motion vectors. Monthly synthetic surface albedo image and a method to reject erroneous correlation vectors were developed. Cloud classification in terms of opacity and height of cloud top is also performed. A whole-sky camera has been used for validation, showing over 85% of agreement between the camera and the satellite derived cloud cover, whereas error in motion vectors is below 15%.

© 2013 Elsevier Ltd. All rights reserved.

1. Introduction

Solar thermoelectric energy has a great potential as an energy supplier in many countries around the world. Solar power plants could play an important role in the next few decades when they become profitable. Whereas solar power technology seems to be developed enough, regarding solar power plant operation there is still room for improvement. Also, the management of the production of thermosolar power plants and the integration of their electricity production involve technological challenges that must be resolved [1].

One possibility to improve solar power plant performance is by forecasting the short-term solar irradiation profile, allowing operators to take decisions on the operation mode, thus optimizing the use of storage systems. Such storage systems (i.e. molten salts) can extend the production of heat beyond the sunlight hours and mitigate the effects of solar radiation natural discontinuities, but their use lead to significant Operations and Maintenance (O&M) challenges [2]. Cloud coverage is the most attenuating factor of beam solar radiation. Predicting when and how long the sun will be covered by clouds would improve solar plant operation. Thus, cloud

detection, cloud classification and cloud motion determination are suggested as the main sources of information for solar plant operation improvement by anticipating the power or thermal storage use.

Some authors study cloud cover through human observations, scoring the clouds portion that covered the sky (oktas) and classifying them according to their appearance. These studies are used when there is no other available source of information (e.g. sky imager, satellite observation) [3]. Sakellariou and Kambezidis (2004) [4] did a prediction of cloud cover using the number of oktas, obtaining satisfactory results.

Cloud cover has been studied too, using satellite images. Satellite images have been used for solar assessment over large areas. Janjai et al. (2009) [5] derived global hourly solar radiation from the visible channel of the Geosynchronous Meteorological Satellite 5 (GMS-5) satellite, while Şenkal and Kuleli [6] utilized Meteosat imagery together with Artificial Neural Networks (ANNs) for the estimation of solar radiation in Turkey. Zarzalejo et al. (2005) [7] developed a model based on ANNs to quantify the influence of the satellite detected clouds on the hourly solar irradiation. More recently, Şenkal (2010) [8] used remote sensing and ANNs to predict global solar radiation without any meteorological data and with a relatively good agreement between measures and predicted values. Also, the prediction of radiance from satellite imagery has served to contrast conventional linear models of estimation of

* Corresponding author. Department of Applied Physics, University of Almería, 04120 Almería, Spain. Tel.: +34 950 015914; fax: +34 950 015477.

E-mail address: fbatlles@ual.es (F.J. Batlles).

radiation, as shown by Olmo et al. (1999) [9] for tilted surfaces. Correlations have been the tool for many researchers for estimating the different components of radiation [10,11]. In the case of Bakirci (2009) [10], different models were analyzed for estimating the monthly average daily global solar radiation on horizontal surface for the provinces of Turkey, extrapolated to another places with similar climatic conditions. Meanwhile, Katiyar and Pandey (2010) [11] studied global radiation behavior in four Indian cities and did a correlation for the entire country with an error lower than 10% with less computational work. The use of empirical models have been compared with ANNs as in the study of Jiang (2009) [12] in China. In this study, Yingni Jiang compares the use of ANN against six theoretical models. A similar work has been developed by Muza-thik et al. (2011) [13], where specific models for horizontal global radiation estimation are compared with each other. An estimation of solar radiation component on tilted surfaces was carried out too using the study proposed by Olmo et al. (1999) [9]. Many researchers have used models to estimate radiation. Six Iranian cities have been analyzed to estimate monthly mean global solar radiation using accurate models. In this case, Khorasanizadeh and Mohammadi (2012) [14] have tried to select the best from 11 models to estimate global radiation for the six cities. In their results, authors show that it is not possible to use an exclusive model that represents well the estimation for the six cities due to the different climate conditions of the analyzed cities. Arid and semiarid climates were studied locally, estimating solar radiation from satellite imagery [15]. Hourly global radiation was estimated by Lu et al. (2011) [16], using images of the visible and infrared bands of the Multi-purpose Transport Satellite (MTSAT) and the Geostationary Operational Environmental Satellite (GOES). Many researchers are working to improve some solar radiation estimation models. This is the case of Voyant et al. (2011) [17]. The authors present here the methodology to determinate the appropriate data input as well as the performance of an ANN for daily global radiation forecast. Short-term solar radiation forecast is based on real-time processing of the satellite images instead of a long-time series analysis. To study cloud motion, it is first necessary to classify cloudy and clear pixels on the images. Several studies utilize multispectral analysis to classify cloudy and clear pixels [18–22]. Other methods have been developed to classify the pixels, many of them based on statistical analysis. Sèze et al. (1985) [23] suggested a four parameter clustering method using visible and infrared channels of Meteosat and their spatial variances. Thiermann and Ruprecht (1992) [24] tried a single infrared channel detection over sea pixels. Simpson and Gobat (1995) [25] developed a split-and-merge clustering method and an adaptive labeling threshold with GOES imagery. Cayula and Cornillon (1996) [26] detected clouds over the sea surface using static temperature gradient and temperature variation in time. Amato et al. (2008) [27] showed that spectral signature of each pixel contains information on the physical characteristics of the land or cloud underlying the pixel, classifying them by comparison with known signatures. Ricciardelli et al. (2008) [28] combined physical, statistical and temporal techniques for cloud detection, using the K-nearest-neighbor method to classify pixels as cloudy or cloudless.

Multispectral analysis is the most known and developed method to detect clouds. In this work, new thresholds for infrared and visible tests based on monthly averaged values are proposed. Synthetic images of mean minimum surface temperature and surface albedo are used to determine the thresholds, following the methodology by Moussu et al. (1989) [29]. Cloud classification is done in terms of both cloud top height and cloud opacity. Cloud top height classifies clouds in low, medium and high. Monthly tropospheric air temperature-height correlation has been done based on sounder data. Nieman et al. (1993) [30] mentions this technique

applied to opaque clouds. Numerical models forecast could be used to determine a height-temperature reference but in this work the input data have been reduced just to the availability of satellite imagery. Additionally, a radiometric study has been done to classify clouds in term of opacity using Meteosat Second Generation (MSG) imagery.

Cloud motion vectors are usually used as an input parameter to feed numerical weather forecast models. However, cloud motion vectors can be used also for solar radiation short-term forecast. Binary cross-correlation is commonly used for cloud tracking and is utilized in this work, applied to the previously detected cloudy pixels [31]. Côte and Tatnall (1995) [32] proposed a Hopfield neural network that improves cloud tracking in rotational motion. Evans (2006) [33] suggested a correlation-relaxation labeling algorithm to make the method more robust. Although other algorithms have been developed, in this work the maximum cross-correlation method is used, which has proven to be a good approach [31,34–36]. Once the image is segmented by sectors and by heights, each sub-matrix is used as a tracer for the tracking correlation. Quality control is performed over the resulting vectors in order to reject incoherent and erroneously detected motions. This paper shows a methodology to determine these three sources of information for short-term prediction of cloudiness. Therefore, this methodology is the first and fundamental step to predict solar radiation in a short time using this type of images.

2. Materials and methods

2.1. Data collection

The following methodology utilizes MSG imagery and no weather forecast fields would be necessary for the short term cloud forecast. Radiometric calibration constants are also needed though they seldom vary. These data are included in the MSG images delivered by EUMETSAT. MSG is a geostationary satellite located at 0° longitude. It takes earth's pictures every 15 min in 11 spectral channels with a 3 km resolution at nadir [37]. Of these 11 MSG channels, five are used in this work (see Table 1) [37].

A 121 × 161 pixel raster image, for every of the five used channels, centered at the University of Almería, is saved and used through the algorithm. This image size covers a ~500 × 500 km² image, large enough for 1 h forecast as the fastest clouds could be detected before they reach the midpoint. Pyrreheliometric data and a whole-sky camera TSI-880 have also been used to test the methodology results. A Kipp&Zonen CH1 pyrreheliometer placed on a Kipp&Zonen 2AP sun tracker has been used to test cloud opacity, whereas a TSI-880 total sky camera has been used to check both cloud cover and cloud motion. Both devices placed at the University of Almería take data every minute.

TSI-880 camera has served for some related task with clouds. For example, Martínez-Chico et al. (2011) [38] used this camera to make a classification of clouds using solar radiation data. Also, aerosols have been analyzed by Gueymard (2005) [39] with this type of camera.

Data from the Kipp&Zonen CH1 pyrreheliometer placed at the PSA-CIEMAT (Solar Platform of Almería [37.5°N 2.2°W]) have also

Table 1
MSG channels used for cloud detection.

Name	Central wavelength (μm)
VIS 0.6	0.635
VIS 0.8	0.81
IR 3.9	3.90
IR 10.8	10.80
IR 12.0	12.00

been used to evaluate cloud opacity. Assuming a tropospheric mean altitude of 15 km, pixels could be treated as slanted columns towards the MSG satellite. The data have been selected for MSG instants where sunbeam goes through just one column-pixel. For 36.83°N and –2.40°E coordinates, sun is limited to [43°,52°] solar altitude and [–8.5°,2.9°] solar azimuth. Thus, a good correlation between pyr heliometrical data and pixel value could be expected, as solar attenuation is due just by only one atmospheric column-pixel.

Satellite cloud detection is hard to compare with ground-based measurements, as no regular cloud detection is done automatically by ground devices. Cloud cover in oktas is usually done by human observers at meteorological stations and airports. Cloud cover will be used as a measure to test cloud detection indirectly. Derrien et al. (1993) [20] also tested this methodology in this respect. A set of 795 skies spread through three months have been visually flagged as cloudless, cloudy and partially cloudy. The proposed detection methodology has been applied to different frame sizes centered at the University of Almería to compare cloud cover results with TSI-880 camera observations. TSI-880 total sky camera has also been used for cloud motion vectors verification.

2.2. Cloud detection tests

The first step before detecting cloudy pixels from satellite imagery is to convert gray levels of the raster image into reflectances (for short-wave channels) and temperatures (for long-wave channels). Once raster image gray levels are converted to radiances, L , using MSG calibration parameters, conversion to reflectance is easily done following EUMETSAT relations [40].

The relation between radiance and temperature used in this work is based on Planck's law:

$$T = \frac{A}{\log(1 + L^B) + C} \quad (1)$$

where T stands for the temperature in Kelvin and A , B and C are constants fitted from T-L tables [40]. Their values and their statistical correlation errors are shown in Table 2.

The correlation factor is represented by R^2 and root mean squared error by RMSE.

Once pixel values represent physical units, multispectral tests could be applied to the images. Reflectance and temperature pixel values, or an algebraic combination of them are compared with different thresholds to tell cloudy from cloudless pixels. A land-sea-coast raster mask is also needed as some thresholds change according to the underlying surface. This surface mask has been obtained from the Satellite Application Facility on support Nowcasting and Very Short Range Forecasting (SAFNWC) atlas dataset.

2.2.1. Literature threshold tests

Four tests from literature have been used in this work unchanged. A snow detection test has been used prior to the other test to avoid misclassification of bright cold snowy cloud free pixels, Derrien and Le Gléau (2010) [41]. Infrared – visible channel ratio test [21], emissivity difference test [19,41] and spatial texture test

[42], have been used according to their references in order to improve cloud detection.

2.2.2. Monthly synthetic raster threshold tests

Two common threshold tests have been improved by replacing spatially constant threshold values for synthetic raster images with specific monthly threshold values for each pixel. This is specially useful in cloud detection over land, as heterogeneity may be high.

2.2.2.1. Visible reflectance threshold test. Two years of image data have been used to compose monthly synthetic raster images of surface albedo. From 1100 to 1300 UTC (higher reflectance hours) every single pixel reflectance from the entire image has been gathered to build a monthly histogram for each pixel. Channel centered at 0.6 μm has been taken for land pixels whereas channel centered at 0.8 μm has been taken for sea pixels as many authors recommend [18,19,41]. Assuming that clouds have a wide spectrum of reflectance values and that surface albedo has a rather constant monthly reflectance, the most repeated value should be the surface albedo. Thus, mode from reasonable albedo interval ([0.1,0.4] for land and [0.0,0.3] for sea) is taken as pixel surface albedo. Fig. 1 shows the surface albedo raster for the month of December.

If reflectance is higher than surface albedo plus an offset (set to 0.08 during this research), a pixel is flagged as cloudy. As short wavelengths have only solar contribution, this test is not applied over pixels where solar zenith angle θ_{sun} is higher than 80°.

2.2.2.2. Infrared temperature threshold test. Two sources have been used to elaborate monthly synthetic rasters of surface temperature. The one for sea pixels is monthly minimum sea surface minimum temperature from the Satellite Application Facility on support to Nowcasting (SAFNWC) database. The one for land pixels is the monthly mean minimum temperature from the Spanish Meteorological State Agency (AEMET) stations. A cubic interpolation and a nearest neighbor extrapolation have been done to fill pixel without values (i.e. missing values, gaps). The 10.8 μm channel temperature value is compared with the monthly mean minimum surface temperature reference of each pixel, T_{min} . If temperature is lower than the minimum value minus an offset, pixel is flagged as cloudy. Offset values can be found in Derrien et al. (1993) [20].

2.3. Opaque cloud tagging

It is of interest to do a qualitative determination of pixel opaqueness and tell which ones are potentially able to obstruct

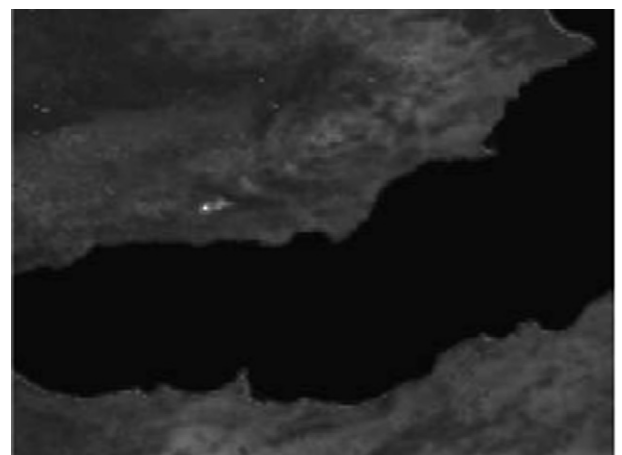


Fig. 1. Synthetic raster of reference surface albedo for the month of December.

Table 2
Constant values and fitted errors for conversion of radiance to temperature.

Channel	A	B	C	R^2	RMSE
IR 3.9	6.016	–0.003316	–0.6731	1	0.0123
IR 10.8	4.817	–0.007258	–0.6601	1	0.0864
IR 12.0	6.29	–0.01058	–0.6468	1	0.1244

solar radiation. It is assumed that opaque clouds would reflect more solar radiation than thin clouds; so they should have a higher value on visible channels reflectance. 247 pyrliometric data have been used for this purpose. Data have been split into two groups: above 400 W m^{-2} (66.7%) and below 400 W m^{-2} (33.3%). Every cloud detection test, some linear combination of them, an opaque cloud test suggested by Derrien and Le Gléau (2010) [41] and cloud top height layer have been compared against each other to find the best way to tag cloudy pixels as opaque ones, potentially able to reduce direct irradiance below 400 W m^{-2} .

2.4. Cloud motion

Due to vertical wind layering and horizontal wind variability, cloud motion vector would be more accurate if it is splitted into different height layers and several raster segments. Clouds could be classified as high, medium, low or convective clouds. As satellite sees only the cloud top, high cumulonimbus would be classified as high cloud. Opaque clouds that could obstruct sunbeam radiation are supposed to be thick enough to avoid earth radiation from below reaching the satellite detector; therefore pixel thermal information could be linked with cloud top temperature and then with cloud top height, assuming thermal equilibrium with its surroundings and comparing its top temperature with air measurements at different altitudes. Sounding air measurements from a weather station in the city of Murcia, close to Almería, have been taken from The University of Wyoming worldwide sounding database to fit a monthly second-order polynomial curve of vertical temperature-height profile [43].

Mean data deviation is 1.0 km and maximum deviation is 1.3 km for the month of April. Based on this result, cloud layers are classified into low, medium and high by the latitude criterion from Stowe et al. (1988) [44].

Raster image is further divided into five horizontal sectors defined around the place of study. Four rectangular sectors are obtained dividing raster image along its two bisections. The fifth sector is the same shape and size as the previous ones, but centered at the center of the raster. Thus, 15 binary matrices (cloud/cloud-free pixel) are generated for one raster image.

2.5. Raster segmentation and binary cross correlation

Three consecutive raster images are used for cloud tracking (image 1, 2 and 3) and one motion vector is determined for each sector and each height. For each sector and height, a maximum cross correlation is performed between images 1 and 2; v_{1-2} vector is obtained as the distance between centers of matching windows, 2 and 3 (v_{2-3}); and 1 and 3 (v_{1-3}). Assuming a steady motion, v_{1-2} and v_{2-3} vectors should be of equal magnitude and phase, and both equal to half of v_{1-3} vector.

To avoid multilayer cloud cover affecting cross correlation, another cross correlation is performed over the non-height-divided image (5 more track vectors, one for each sector). Moreover, to avoid outgoing clouds affecting individual cross correlation, the entire raster image is also correlated (3 + 1 more track vectors, one for each height and one more for the non-height-divided image). Finally, to avoid border fading effects, eroded images are also correlated for each sector and height (15 + 5 + 4 more track vectors). As a result, 48 cross correlation vectors are computed from the 3 raster images.

Each vector is calculated as the average

$$V = \frac{v_{1-2} + v_{2-3}}{2} \quad (2)$$

if it is accomplished that:

$$\begin{aligned} ||v_{1-2}| - |v_{2-3}|| &\leq 10 \text{ m s}^{-1} \\ |\phi_{1-2} - \phi_{2-3}| &\leq 20^\circ \\ ||2V| - |v_{1-3}|| &\leq 20 \text{ m s}^{-1} \\ |\phi - \phi_{1-3}| &\leq 40^\circ \end{aligned} \quad (3)$$

where ϕ_{i-j} is the angle between vectors i and j , or if vectors are small enough:

$$\begin{aligned} |v_{1-2}| &\leq 10 \text{ m s}^{-1} \\ |v_{2-3}| &\leq 10 \text{ m s}^{-1} \\ |v_{1-3}| &\leq 10 \text{ m s}^{-1} \\ |V| &\leq 10 \text{ m s}^{-1} \end{aligned} \quad (4)$$

without considering their phase ϕ . If v_{1-2} , v_{2-3} and v_{1-3} satisfy Eqs. (3) or (4), then V is a coherent vector. If they do not, then an error code is assigned to V . Once the 48 vectors are flagged as coherent or filled with error codes, six quality tests are applied over them to choose the proper cloud tracking vector for each height and sector.

- First test deletes erroneous vectors caused by border fading. If vectors from eroded images of a particular height are equal to zero for the five sectors, vectors from non-eroded images are considered invalid.
- Then, if vector from the non-eroded image is invalid and the corresponding one from the eroded image is not, the last one is taken as the proper cloud vector.
- If vectors from eroded and non-eroded images differ by more than 20 m s^{-1} modulus or 40° phase, both are considered invalid vectors.
- If no valid vector is available for a particular sector and a particular height, vector from the entire image correlation of the same height is chosen as the proper vector for this sector.
- If there is no spatial coherence (considering both modulus and phase) between vectors from different sectors of the same height, vector from entire image at the same height is chosen as proper vector for the different sector or sectors. There should be at least three coherent sectors.
- If a vector from the entire image is not valid, vector from the non-height-divided image is taken for the needed sector.

At last, if no vector could be used for a particular sector and height, the last one from the previous cloud track determination is used.

3. Results

Results from cloud detection, opaque cloud tagging and cloud tracking are detailed in this section. Cloud top height comparison would need an atmospheric sounder co-located with the cloud and a parallel device to infer if there is a cloud in the direction where it is detected by satellite. A ceilometer would not be enough by itself as it measures cloud bottom height whereas satellite estimates cloud top height.

3.1. Cloud detection

A total of 795 MSG satellite images have been processed and clouds have been detected by the algorithm described. These images correspond to April, July and October of 2010. They are representative months of spring, summer and autumn, respectively. In parallel, TSI-880 images from the whole-sky camera placed at the University of Almería have been analyzed. The 10-min delay between slot time and MSG satellite radiance acquisition time over the

South of Spain should be taken into account to compare satellite images and whole-sky pictures; otherwise, they would show different time instants. By visual inspection, TSI-880 images have been classified into three groups: cloudless sky, overcast and partially cloudy, taking into account the measurement of cloud cover in oktas. Meanwhile, cloud detection results are saved automatically for several frame sizes centered at the University of Almería. These frame sizes vary from 5×7 to 13×17 pixels. Considering an average pixel size of $4.2 \times 3 \text{ km}^2$, frames cover from 21×21 to $54.6 \times 51 \text{ km}^2$. Different frame sizes are needed due to the whole-sky camera horizon uncertainty. Cloudy pixels on the frame are compared with total number of pixels and situations are also divided into three categories: cloudless, if the number of cloudy pixels is below $1/8$ of the total pixel amount; overcast if it is over $7/8$, and partially cloudy otherwise.

Comparing cloud cover situations is an indirect way to test cloud detection. As the amount of clouds is directly proportional to the detected clouds, agreement in sky cover type could be used as agreement in cloud detection. Comparison between the whole-sky camera and satellite imagery could lead to wrong conclusions due to the following causes, all related to cameras hemispherical geometry: camera's horizon (high clouds appear sooner in whole sky images than low clouds at the same distance, whereas height does not affect satellite imagery). Camera's oktas determination (a small low cloud could fill more scene than a big high cloud whereas cloud size is not relative to the height in satellite images). Cloud visual transparency (high semitransparent cirrus could be undetected in the visual inspection whereas they are supposed to be detected by the test algorithm). Multiple cloud layers (contrast in whole-sky camera may lead to a sky misclassification). Fig. 2 shows coincidence percentage between both visual and automatic sky classifications for a 9×11 pixel frame centered at the University of Almería. It is worth pointing out that cloud detection algorithm always detects clouds in overcast situations (0% of MSG cloudless and TSI-880 overcast) and never fills the frame with clouds in cloudless situations (0% of MSG overcast and TSI-880 cloudless).

Cloudless and overcast skies are well identified by detection algorithm as there is more than a 90% of agreement with visual classification in both situations. Partially cloudy skies show a 75% of

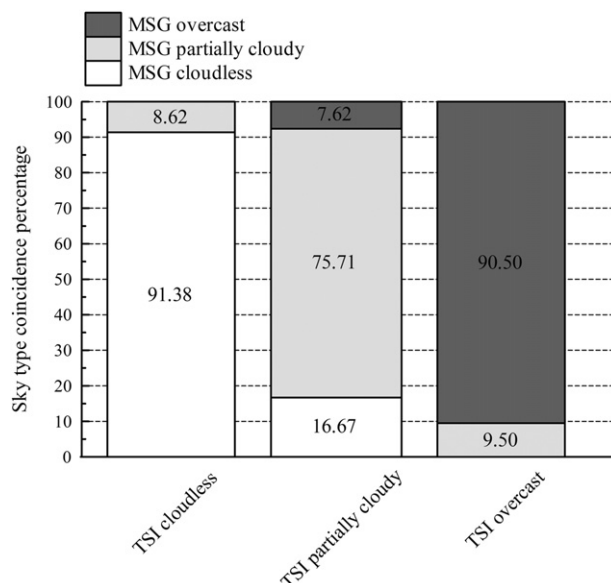


Fig. 2. Percentage of correct sky type situation for a 9×11 frame pixel size.

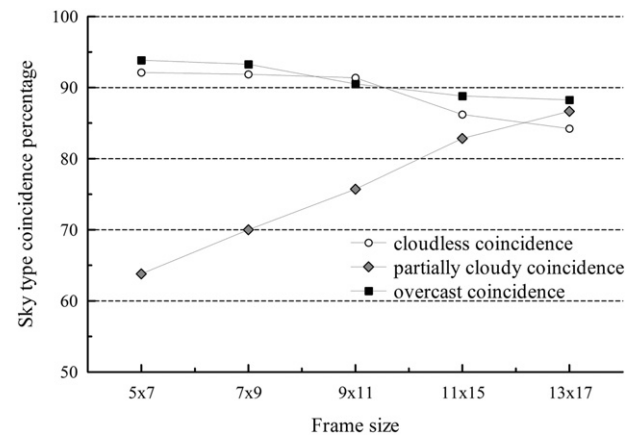


Fig. 3. Sky type coincidence percentage for several frame sizes.

coincidence percentage. Thus, it is inferred that the sky type is well defined by the MSG satellite cloud detection algorithm.

Fig. 3 shows sky type coincidence percentage for different frame sizes. As the frame gets bigger, more clouds can enter it and cloudy pixel rate can become higher than $1/8$, reaching the partially cloudy oktas interval. Thus, distant high clouds can appear on the whole-sky camera but in a small frame, this is why partially cloudy type may become better for larger frames.

3.2. Opaque cloud tagging

Fig. 4 shows the percentage of detection test results in cases where direct irradiance is over and below 400 W m^{-2} .

It can be seen that the visible test detects 91.5% of opaque clouds. A 15.2% of pixel situations when beam radiation exceeds 400 W m^{-2} is also detected by this test. Although there is a high misclassification rate, opaque clouds over-detection is preferable for power plant operation warnings. In addition, many of these situations could be caused by small or broken cumulus clouds that may allow beam radiation to reach ground between their empty spaces or holes.

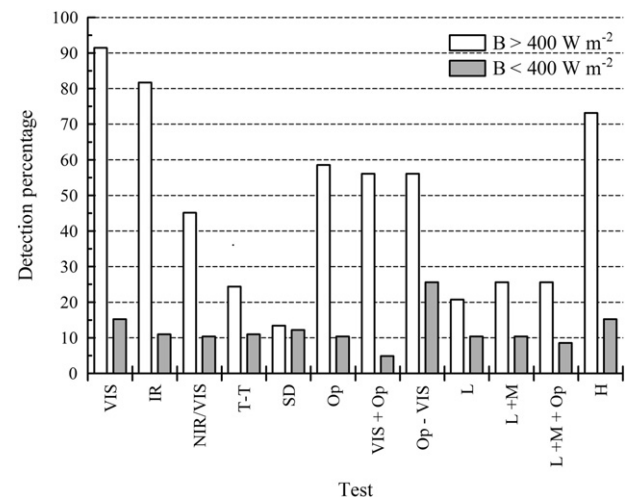


Fig. 4. Different detection tests percentage. VIS, IR, NIR/VIS, T-T and ST stand for visible, infrared, ratio, difference and spatial texture test detection respectively. Op stands for the opaque pixel test proposed by Derrien and Le Gléau (2010) [41], which shows uniformly covered pixels from non-uniformly covered pixels. L, M and H stand for low, medium and high cloud top height, respectively.

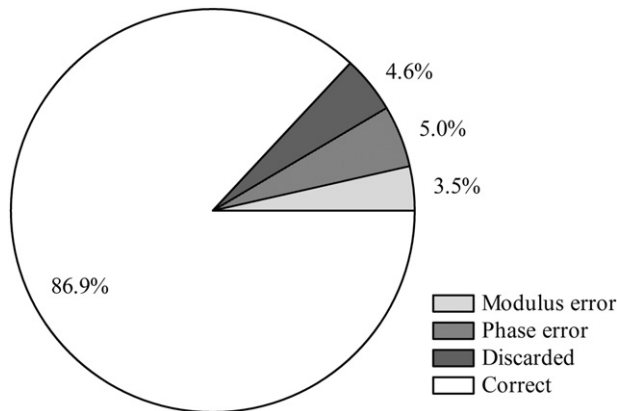


Fig. 5. Average error pie.

3.3. Cloud tracking

A total of 11,250 estimated vectors have been calculated for the cloud tracking method evaluation. They correspond to 120 days of 5 different months, January, February, April, July and October of 2010, from 0900 to 1500 UTC. Visual check on consecutive satellite processed images and TSI-880 pictures has been made to verify resulting vectors at different heights and in different sectors. Three kinds of error may be found: modulus error, phase error or rejected vector by quality tests. These rejected vectors are considered errors because the inability of the method to provide a motion vector while cloud motion is observed. On real-time operation, previous vector for the same height and sector could be used as tropospheric wind is assumed to be rather steady, reducing the total error percentage. Fig. 5 shows checked errors pie graph. One can see the high percentage of right tracking vectors, higher than 85%. Discarded vectors add a 4.6% error.

Cloud tracking error is therefore around 10%. Fig. 6 analyzes the error contribution of different cloud heights. Low clouds, which usually are the most opaque, have a little contribution to the total error. Direction errors are the major contribution to the total error though they are mostly due to high clouds.

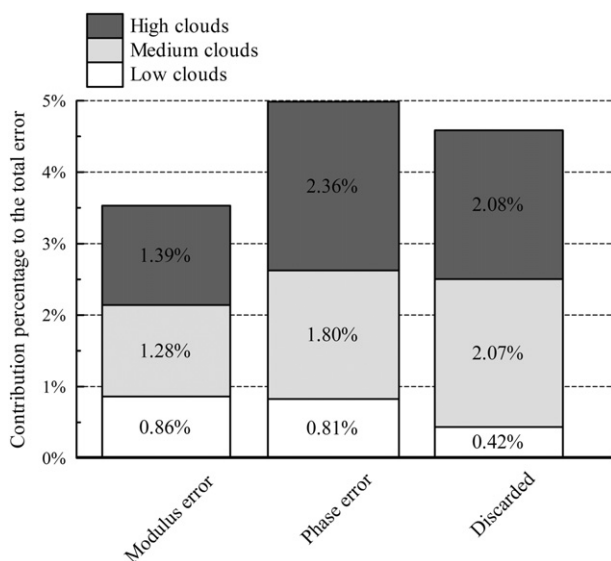


Fig. 6. Height error contribution.

4. Conclusions

It has been pointed out that cloud detection, cloud classification and cloud motion determination are required for the forecast of cloud cover. These three tasks and short term cloud forecast could be solely performed by multispectral satellite imagery. Multispectral analysis is needed to detect clouds and classify them in terms of top height and opacity. Specifically, infrared channels are essential for cloud height assignment and visible channel is necessary for cloud opacity determination. It has been obvious that visible channels are remarkably important to detect thick clouds due to their high reflectance. Thus, an effort has been made to define proper pixel thresholds that would take into account ground heterogeneity.

Cloud cover agreement has been used to infer cloud detection results. Some authors check detection results with different detection algorithms [19,42], which might include detection errors as well. Other authors check their results with SYNOP observations [20,22]. Here a whole-sky imager has been taken as reference. Comparison between both sources is not ideal due to their different projections and fields of view. However, results show an agreement above 90% between satellite detected and observed cloud cover for cloudless and overcast situations, and over 75% for partially cloudy skies.

Binary cross-correlation method has been chosen to estimate cloud motion vectors. Coherence and quality test over cloud motion vectors are quite significant as they reject many cross-correlation failures. Results show that over 86% of the motion vectors are well determined. High clouds have a significant contribution to the error but many of them would not affect sun shading predictions as they are thin clouds with low opacity.

This work represents the starting point for addressing the prediction of solar radiation to short time using satellite imagery.

Acknowledgments

This research has been conducted with the support of the project *Gemasolar* Project, financed by CDTI (IDI-20091384) and Torresol Energy Investments S.A. This study has also been carried out with the help of the project CGL2011-30377-C02-02, financed by the Ministerios de Ciencia e Innovación, today called Ministerio de Economía y Competitividad.

References

- [1] Zidanšek A, Ambrožič M, Milfelner M, Blinc R, Lior N. Solar orbital power: sustainability analysis. *Energy* 2011;36:1986–95.
- [2] Cavallaro F. Fuzzy TOPSIS approach for assessing thermal-energy storage in concentrated solar power (CSP) systems. *Applied Energy* 2010;87(2):496–503.
- [3] Robaa SM. Evaluation of sunshine duration from cloud data in Egypt. *Energy* 2008;33:789–95.
- [4] Sakellariou N, Kambezidis H. Cloud cover in the Athens area, Greece. *Fresenius Environmental Bulletin* 2004;13(1):66–8.
- [5] Janjai S, Pankaew P, Laksanaboonsong J. A model for calculating hourly global solar radiation from satellite data in the tropics. *Applied Energy* 2009;86(9):1450–7.
- [6] Şenkal O, Kuleli T. Estimation of solar radiation over Turkey using artificial neural network and satellite data. *Applied Energy* 2009;86(7–8):1222–8.
- [7] Zarzalejo LF, Ramírez L, Polo J. Artificial intelligence techniques applied to hourly global irradiance estimation from satellite-derived cloud index. *Energy* 2005;30:1685–97.
- [8] Şenkal O. Modeling of solar radiation using remote sensing and artificial neural network in Turkey. *Energy* 2010;35:4795–801.
- [9] Olmo FJ, Vida J, Foyo I, Castro-Díez Y, Alados-Arboledas L. Prediction of global irradiance on inclined surfaces from horizontal global irradiance. *Energy* 1999;24:689–704.
- [10] Bakirci K. Correlations for estimation of daily global solar radiation with hours of bright sunshine in Turkey. *Energy* 2009;34:485–501.
- [11] Katiyar A, Pandey CK. Simple correlation for estimating the global solar radiation on horizontal surfaces in India. *Energy* 2010;35:5043–8.

- [12] Jiang Y. Computation of monthly mean daily global solar radiation in China using artificial neural networks and comparison with other empirical models. *Energy* 2009;34:1276–83.
- [13] Muzathik A, Ibrahim M, Samo K, Nik WW. Estimation of global solar irradiation on horizontal and inclined surfaces based on the horizontal measurements. *Energy* 2011;36:812–8.
- [14] Khorasanizadeh H, Mohammadi K. Introducing the best model for predicting the monthly mean global solar radiation over six major cities of Iran. *Energy* 2012. <http://dx.doi.org/10.1016/j.energy.2012.11.007>.
- [15] Sabziparvar AA, Shetaee H. Estimation of global solar radiation in arid and semi-arid climates of East and West Iran. *Energy* 2007;32:649–55.
- [16] Lu N, Qin J, Yang K, Sun J. A simple and efficient algorithm to estimate daily global solar radiation from geostationary satellite data. *Energy* 2011;36:3179–88.
- [17] Voyant C, Muselli M, Paoli C, Nivet ML. Optimization of an artificial neural network dedicated to the multivariate forecasting of daily global radiation. *Energy* 2011;36:348–59.
- [18] Saunders RW. An automated scheme for the removal of cloud contamination from AVHRR radiances over western Europe. *International Journal of Remote Sensing* 1986;7(7):867–86.
- [19] Saunders RW, Kriebel KT. An improved method for detecting clear sky and cloudy radiances from AVHRR data. *International Journal of Remote Sensing* 1988;9(1):123–50.
- [20] Derrien M, Farki B, Harang L, LeGléau H, Noyalet A, Pochic D, et al. Automatic cloud detection applied to NOAA-11/AVHRR imagery. *Remote Sensing of Environment* 1993;46(3):246–67.
- [21] Chen PY, Srinivasan R, Fedosejevs G, Narasimhan B. An automated cloud detection method for daily NOAA-14 AVHRR data for Texas, USA. *International Journal of Remote Sensing* 2002;23(15):2939–50.
- [22] Kriebel KT, Gesell G, Kästner M, Mannstein H. The cloud analysis tool APOLLO: improvements and validations. *International Journal of Remote Sensing* 2003;24(12):2389–408.
- [23] Sêze G, Belcour C, Desbois M. Cloud cover analysis using spectral and spatial characteristics of meteosat images. *Advances in Space Research* 1985;5(6):165–8.
- [24] Thiermann V, Ruprecht E. A method for the detection of clouds using AVHRR infrared observations. *International Journal of Remote Sensing* 1992;13(10):1829–41.
- [25] Simpson JJ, Gobat JL. Improved cloud detection in GOES scenes over land. *Remote Sensing of Environment* 1995;52(1):36–54.
- [26] Cayula JF, Cornillon P. Cloud detection from a sequence of SST images. *Remote Sensing of Environment* 1996;55(1):80–8.
- [27] Amato U, Antoniadis A, Cuomo V, Cutillo L, Franzese M, Murino L, et al. Statistical cloud detection from SEVIRI multispectral images. *Remote Sensing of Environment* 2008;112(3):750–66.
- [28] Ricciardelli E, Romano F, Cuomo V. Physical and statistical approaches for cloud identification using Meteosat Second Generation-Spinning Enhanced Visible and Infrared Imager Data. *Remote Sensing of Environment* 2008;112(6):2741–60.
- [29] Moussu G, Diabate L, Obrecht D, Wald L. A method for the mapping of the apparent ground brightness using visible images from geostationary satellites. *International Journal of Remote Sensing* 1989;10(7):1207–25.
- [30] Nieman SJ, Schmetz J, Menzel WP. A comparison of several techniques to assign heights to cloud tracers. *Journal of Applied Meteorology* 1993;32(9):1559–68.
- [31] Leese JA, Novak CS, Taylor VR. The determination of cloud pattern motions from geosynchronous satellite image data. *Pattern Recognition* 1970;2(4):279–92.
- [32] Côté S, Tatnall A. A neural network-based method for tracking features from satellite sensor images. *International Journal of Remote Sensing* 1995;16(18):3695–701.
- [33] Evans A. Cloud motion analysis using multichannel correlation-relaxation labeling. *Geoscience and remote sensing letters. IEEE* 2006;3(3):392–6.
- [34] Rutledge G, Legg E, Menzel P. Operational production of winds from cloud motions. *Global and Planetary Change* 1991;4(13):141–50.
- [35] Laurent H. Wind extraction from meteosat water vapor channel image data. *Journal of Applied Meteorology* 1993;32(6):1124–33.
- [36] Schmetz J, Holmlund K, Hoffman J, Strauss B, Mason B, Gaertner V, et al. Operational cloud-motion winds from meteosat infrared images. *Journal of Applied Meteorology* 1993;32(7):1206–25.
- [37] Schmetz J, Pili P, Tjemkes S, Just D, Kerkmann J, Rota S, et al. An introduction to Meteosat Second Generation (MSG). *Bulletin of the American Meteorological Society* 2002;83(7):977–92.
- [38] Martínez-Chico M, Batlles FJ, Bosch JL. Cloud classification in a mediterranean location using radiation data and sky images. *Energy* 2011;36:4055–62.
- [39] Gueymard CA. Importance of atmospheric turbidity and associated uncertainties in solar radiation and luminous efficacy modelling. *Energy* 2005;30:1603–21.
- [40] EUMETSAT. Effective radiance and brightness temperature relation for meteosat 8 and 9; 2009. EUM/OPS-MSG/TEN/08/0024. Available online.
- [41] Derrien M, Le Gléau H. Algorithm theoretical basis document for “Cloud products” (CMA-PGE01 v3.0, CT-PGE02 v2.0 & CTTH-PGE03 v2.1); 2010. Available online.
- [42] Derrien M, Le Gléau H. MSG/SEVIRI cloud mask and type from SAFNWC. *International Journal of Remote Sensing* 2005;26(21):4707–32.
- [43] University of Wyoming, Department of Atmospheric Science; 2011. <http://weather.uwyo.edu/upperair/sounding.html>.
- [44] Stowe LL, Wellemeyer CG, Yeh HYM, Eck TF. Nimbus-7 global cloud climatology. Part I: algorithms and validation. *Journal of Climate* 1988;1(5):445–70.